Research Square

Preprints are preliminary reports that have not undergone peer review.
They should not be considered conclusive, used to inform clinical practice,
or referenced by the media as validated information.

Secondary Flow Injection for Thrust Vectoring in Convergent–Divergent Nozzles: A Comprehensive Review of Flow Physics and Design Strategies

Deepak Gupta
Lovely Professional University
Amit Kumar Thakur
Lovely Professional University
Balaji Ravi
balaaero07@gmail.com

Lovely Professional University

Research Article

Keywords: Fluidic thrust vectoring, Secondary flow injection, Convergent–divergent nozzle, Shock vector control, Dual-throat nozzle, Throat shifting, Momentum flux ratio, Supersonic jet interaction, Boundary-layer separation, non-mechanical thrust control

Posted Date: August 14th, 2026

DOI: https://doi.org/10.21203/rs.3.rs-10653015/v1

License: This work is licensed under a Creative Commons Attribution 4.0 International License.
Read Full License

Additional Declarations: No competing interests reported.

Secondary Flow Injection for Thrust Vectoring in Convergent–Divergent Nozzles: A Comprehensive Review of Flow Physics and Design Strategies

Deepak Gupta[1], Amit Kumar Thakur[2*], Balaji Ravi[3]

[1]Research Scholar, Department of Aerospace, Lovely Professional University, Phagwara, Punjab -144401

[2,3]Department of Aerospace, Lovely Professional University, Phagwara, Punjab -144401

Abstract

Fluidic thrust vectoring (FTV) via secondary flow injection offers a lightweight, non-mechanical alternative to conventional thrust vector control by exploiting shock-flow interactions, asymmetric pressure fields, and boundary-layer separation within convergent-divergent nozzles. This comprehensive review synthesizes over 150 peer-reviewed articles, bridging classical fundamentals with recent advancements from 2021 to 2025. We systematically analyze governing flow physics, critical non-dimensional parameters—including nozzle pressure ratio (NPR), secondary pressure ratio (SPR), and momentum flux ratio—and the comparative performance of mechanisms such as shock vector control, throat shifting, and the Coanda effect. Crucially, the review assesses experimental and computational approaches, highlighting the pivotal role of unsteady RANS (URANS) and reacting flow simulations in accurately predicting transient vectoring behavior and unsteady side loads. Addressing persistent challenges like thrust penalties and high-NPR scalability, we emphasize the emergence of hybrid fluidic concepts and high-fidelity optimization approaches as the definitive framework for developing next-generation FTV systems for supersonic, hypersonic, and reusable launch vehicles.

Keywords: Fluidic thrust vectoring; Secondary flow injection; Convergent–divergent nozzle; Shock vector control; Dual-throat nozzle; Throat shifting; Momentum flux ratio; Supersonic jet interaction; Boundary-layer separation; non-mechanical thrust control

Nomenclature

Symbol	Description	Units
(A_t)	Nozzle throat area	m^2
(A_e)	Nozzle exit area	m^2
(C_f)	Thrust coefficient	–
(C_y)	Side-force coefficient	–
(D_t)	Nozzle throat diameter	m
(D_j)	Injector jet diameter	m
(E)	Total energy per unit mass	J/kg
(F)	Thrust with secondary injection	N
(F_o)	Baseline thrust without injection	N
(F_x)	Axial thrust component	N
(F_y)	Lateral force component	N
(J)	Momentum flux ratio	–
(k)	Turbulent kinetic energy	m^2/s^2
(NPR)	Nozzle pressure ratio ($P_{0,p}/P_a$)	–
(P_a)	Ambient pressure	Pa
($P_{o,p}$)	Primary total pressure	Pa
($P_{o,s}$)	Secondary total pressure	Pa
(P_k)	Turbulence production term	m^2/s^3
(Re)	Reynolds number	–
(R_c)	Wall curvature radius	m
(SPR)	Secondary pressure ratio ($P_{0,s}/P_{0,p}$)	–
(T)	Temperature	K
(TR)	Thrust ratio ((F/F_0)	–
(U_p)	Primary jet velocity	m/s
(U_s)	Secondary jet velocity	m/s
($\dot{m}$p)	Primary mass flow rate	kg/s
($\dot{m}$s)	Secondary mass flow rate	kg/s
(δ)	Thrust vector angle	deg
($\boldsymbol{\eta}_v$)	Thrust vectoring efficiency	deg/%
($\boldsymbol{\nu}$)	Kinematic viscosity	m^2/s
($\boldsymbol{\nu}_t$)	Turbulent eddy viscosity	m^2/s
($\boldsymbol{\rho}_p$)	Primary flow density	kg/m^3
($\boldsymbol{\rho}_s$)	Secondary flow density	kg/m^3
($\boldsymbol{\omega}$)	Specific dissipation rate	1/s
($\boldsymbol{\phi}$)	Viscous dissipation	W/m^3
($\boldsymbol{\tau}$)	Viscous stress tensor	Pa

1. Introduction

Thrust vector control (TVC) is a critical technology used in advanced propulsion systems that facilitates vehicle maneuverability. This is particularly true when flying in environments where aerodynamic control is limited. These environments include low dynamic pressures and large angles of attack. TVC is commonly used in fighter aircraft, missiles, and space vehicles. Traditional TVC systems utilize mechanical systems such as gimbaling motors and nozzles. Although they are effective solutions, they are heavy and complicated. This makes them unsuitable for advanced aerospace vehicles that demand high efficiencies [1-4]. Fluidic thrust vectoring provides a non-mechanical alternative by controlling the direction of the jets by injecting secondary flows into the main exhaust stream. This generates asymmetric shocks, pressure distribution, and boundary layer separation, resulting in a side force that deflects the jet. The injected flow is equivalent to an obstruction for the supersonic main stream, thus allowing flow turning [5]. The secondary flow injections in convergent-divergent (C-D) nozzles have been commonly examined for simplicity and suitability for fixed-geometry configurations. Research has demonstrated that optimized secondary flow injections can attain thrust vector angles between 15° and 17° with secondary mass flows below 10% and thrust ratios greater than 0.94, similar to mechanical system performance with additional advantages in weight reduction and improvement in system reliability [10–13]. Nevertheless, FTV performance is controlled by intricate interactions such as jet-crossflow interactions, shock-boundary layer interactions, and asymmetrical separations, and is significantly affected by various parameters such as NPR, SPR, momentum ratio, and configuration, resulting in a multi-dimensional design trade space [14–16]. One recent concept of co-flow FTV for low-speed UAVs involves a high-speed secondary jet injected into the boundary layer of the primary jet to deflect the exhaust and produce a pitch control without the need for surfaces. Experiments and CFD validation have confirmed that the concept can produce a vertical force of ~0.4 N at a primary speed of 19 m/s and a deflection of ~25° for the jet, thereby achieving effective vectoring at a small scale [6]. Although much has been studied in the field of fluidic thrust vectoring in the last few decades, the existing literature presents a diverse range of different approaches, geometries, and conditions used in the study of fluidic thrust vectoring. Recent developments in high-fidelity CFD, reacting flow simulation, and optimization techniques have also further broadened the scope of fluidic thrust vectoring to

supersonic, hypersonic vehicles, and reusable vehicles, making it essential to develop a unified synthesis of the underlying physics and design approaches [17-20]. Experimental results obtained for an axisymmetric M = 2 C–D nozzle at NPR = 5 emphasize the role of injection location. In this case, negligible deflection is observed at L_s=0.5L_d due to shock reflection. However, if injection is used at 0.75L_d, deflection is obtained at 5.5° and 10° at SPR = 0.5, 1.0, and 1.5 with a corresponding loss in thrust of 11–13%[7]. The purpose of this review is to systematically synthesize and critically discuss secondary injection-based FTV in C–D nozzles using classical and recent literature (2021–2025) to create a framework that connects flow physics and performance with nozzle design.

In this current research work, we systematically analyze over 150 peer-reviewed articles to bridge classical fluidic thrust vectoring (FTV) fundamentals with recent advancements spanning from 2021 to 2025. The study critically examines governing flow physics alongside crucial non-dimensional parameters—specifically the nozzle pressure ratio (NPR), secondary pressure ratio (SPR), and momentum flux ratio. Furthermore, it provides a comparative performance assessment of key vectoring mechanisms, including shock vector control, throat shifting, and the Coanda effect. By assessing both experimental techniques and high-fidelity computational approaches, such as unsteady RANS (URANS) and reacting flow simulations, this review highlights the prediction of transient vectoring behaviors and unsteady side loads. Ultimately, this work addresses persistent operational challenges, such as thrust penalties and high-NPR scalability, establishing a definitive framework focused on hybrid fluidic concepts and optimization strategies for developing next-generation FTV systems applicable to supersonic, hypersonic, and reusable launch vehicles

2. Historical Evolution of Fluidic Thrust Vectoring

The history of fluidic thrust vectoring using secondary flows can be traced back over more than six decades. Research conducted in the 1950s and 1960s showed that injection of secondary flows across supersonic exhaust streams creates an oblique shockwave and increases local pressure, resulting in lateral control [21, 22]. Research conducted in the 1960s and 1970s focused on understanding the physics of fluidic thrust vectoring. This research demonstrated that bow shockwave formation, shockwave propagation, and shockwave boundary layer interaction are

critical aspects of fluidic thrust vectoring. Moreover, this research demonstrated that fluidic thrust vectoring is not a momentum exchange problem but rather a problem related to asymmetry in pressure [23–25]. In the 1980s–1990s, research focused on structured concepts, such as shock vector control (SVC), where injection in the divergent section creates oblique shocks near the exit for sustained deflection. At the same time, throat-shifting and sonic-plane-skewing concepts were developed, proving that injecting near the throat could shift the sonic line and generate asymmetric separation, thus improving vectoring efficiency [26–30]. In the late 1990s and early 2000s, computational fluid dynamics (CFD) emerged, where RANS-based CFD simulations allowed for parametric investigations of injectors. This period saw the introduction of dual-throat nozzle concepts, where separation control was improved, and vectoring efficiency was achieved for angles above 12–17 degrees, with moderate thrust penalties [31–36]. From 2010 onwards, research has been directed toward optimization and hybridization approaches that utilize a combination of mechanisms like SVC and throat shifting. Sophisticated simulation tools like URANS have made it possible to analyze transient issues, side loads, and control integration that are essential for field applications [37-40]. Recent research activities (2021-2025) are directed toward high-fidelity simulations, reacting flows, and applications for supersonic/hypersonic vehicles and reusable systems. Activities are also directed toward fuel-based injection, multi-objective optimization, and scaling performance at high NPR values. In addition, experimental research is conducted to improve efficiency and stability. It is evident that FTV research has matured to a level that can support a non-mechanical control technology for future generations of aircraft systems [41-44].

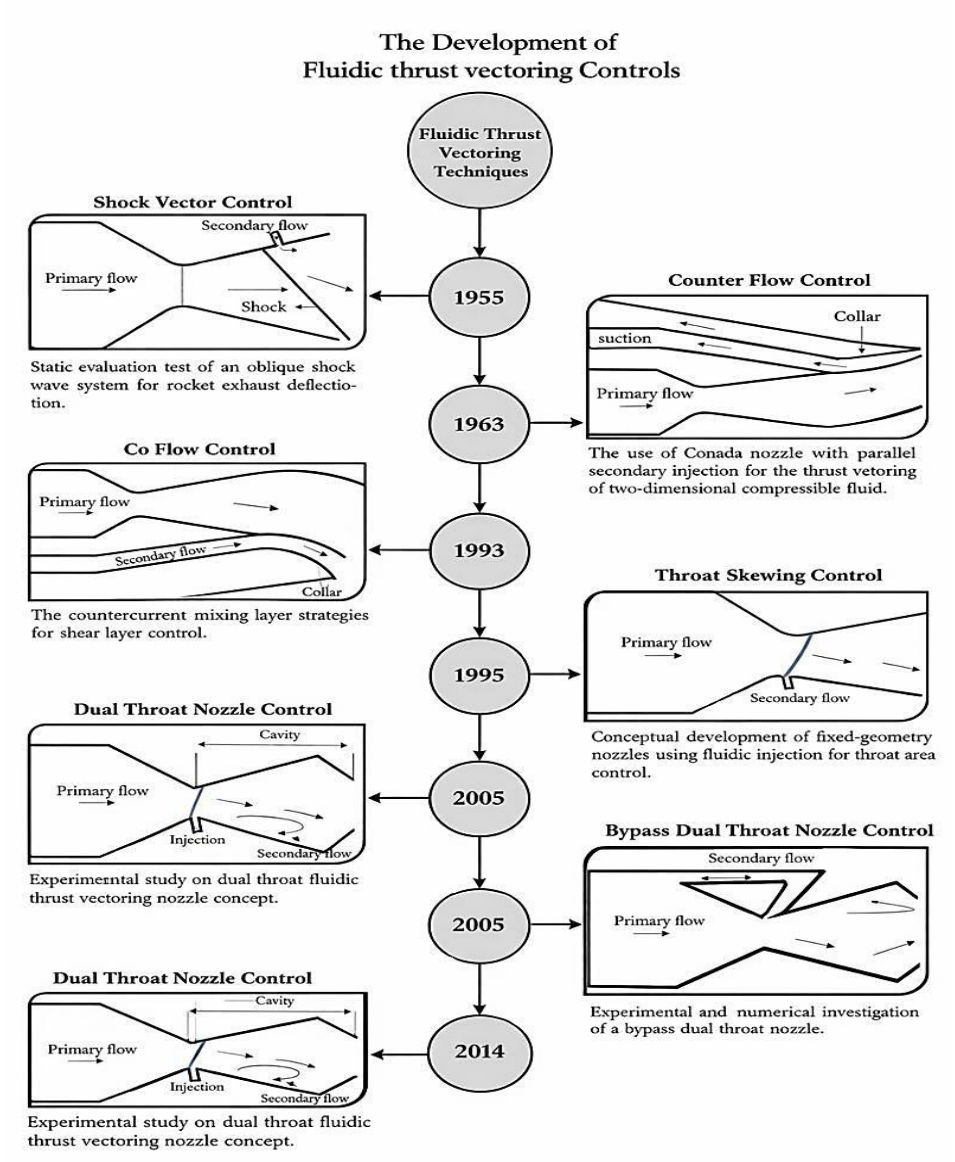


Figure 1. History of fluidic thrust vectoring controls techniques[8].

The figure 1 presents an overview of the evolution from initial transverse injection concepts (1950s-1960s) to structured concepts such as shock vector control and throat shifting (1980s-1990s), and further to dual-throat nozzles and CFD optimization (2000s-2010s). The recent developments (2021-2025) include high-fidelity simulations, hybrid methods, and system integration for advanced aerospace concepts [21-44].

3. Thrust Vectoring Methods and Configurations

Thrust vectoring is used for controlling vehicle motion by deflecting exhaust gases. This capability is critical for environments where aerodynamic control is limited. Thrust vectoring can be achieved through mechanical means, such as gimbals and vanes, which offer high authority but introduce added weight, complexity, and maintenance issues. Fluidic thrust vectoring provides a non-mechanical alternative, offering improved reliability and compactness, albeit with lower overall efficiency. In these systems, flow asymmetry is achieved entirely inside the nozzle. The primary fluidic methods explored in the literature include shock vector control, throat-shifting nozzles, the Coanda effect, and hybrid vectoring combinations.

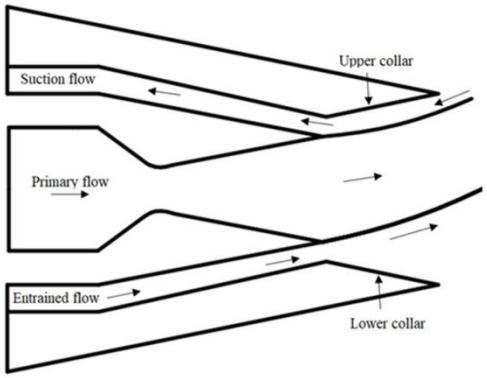


Figure 2. Schematic of collar-assisted secondary flow entrainment and interaction with the primary jet.

3.1 Shock Vector Control (SVC)

Shock Vector Control (SVC) is a structured fluidic vectoring concept where secondary flow is injected into the divergent section of the nozzle. The dominant physical phenomenon in SVC is oblique shock impingement and the resulting pressure asymmetry. The injection creates oblique shocks near the nozzle exit, leading to sustained deflection of the primary exhaust stream. Maximum vectoring is typically observed when the induced oblique shock strikes the opposite nozzle wall near the exit, a condition consistent with separated SVC states.

3.2 Performance is highly dependent on injection location and the nozzle pressure ratio (NPR):

Separation Dynamics: In planar SVC configurations (e.g., $H = 27.5$ mm, $A_e/A_t = 1.8$, $R_j = 2$ mm, $5 \leq NPR \leq 20$, $m_j/m_p = 2.1\% - 12.2\%$), separation generally occurs downstream of the injection point [14]. Partial flow reattachment limits the vector angle to a few degrees under certain conditions (such as $NPR = 10$, $x_j/L = 0.8$, and a secondary mass flow ratio of 4.2%) [14].

Injection Positioning: Moving the injection point upstream ($x_j/L = 0.7 - 0.9$) shifts the separation region closer to the injection slot [14]. This modification increases the vector angle (exceeding 10°) but consequently increases thrust loss [14]. Over-expansion at lower NPRs (e.g., $NPR = 5$) amplifies these separation effects [14].

Bypass Ratio: Increasing the bypass ratio at a fixed $NPR = 10$ moves the separation upstream and enlarges the plateau region, which monotonically increases the vector angle while simultaneously reducing the thrust ratio and specific impulse [14]. Practical vectoring is generally limited to approximately 10° for bypass ratios below 10% [14].

Table 1. Literature review analysis on Secondary flow parameters

Study / nozzle concept	Key geometry / operating range	Secondary-flow parameter	Main quantitative outcomes
[10]	H_2–O_2, pc≈200 bar, Rt≈0.07 m, εb=30, ε0=100	None (pure dual-bell)	h≈15,000 m (pamb≈0.18 bar), pw,e≈0.18 bar; off-design losses up to ~15% (conventional), reduced in dual-bell
[11]	Dual-bell, Rt=0.1 m, εb=48, ε0=115, pc=12 MPa, Tc≈3500 K	Slot at x/Rt=10, s/Rt=0.08–0.11, β=0.029–0.059, Mf=1–2	Tw,exit≈3363 K → >1060 K (β=0.059, Mf=2); film-break x/Rt=13–14; li/Rt: 3.8→5.5; side-load ↑20–40%
[12][10]	Sub-scale H_2–O_2, TOP vs TIC (same pc, ε)	None (FSS/RSS focus)	TIC side load ≈33.3% of TOP; TOP shows FSS→RSS; TICTOP keeps pw,e≈0.4 bar (pc/pamb≈555), delays separation
[15]	2D BDTN: ht=20 mm, Lc≈3.34ht, channel=0.185ht, Ae/At=1.2, 2≤NPR≤10	Internal bypass ≈6%	NPR=10: θv=21.3°, CF/CF,0=0.97 (~3% loss); best near NPR≈4; θv≈27° at NPR=3 (CFD)
[14]	2D CD: L=57.8 mm, H=27.5 mm, Ae/At=1.8; Rj=2 mm, xj/L=0.7–0.9	mj/mp=2.1–12.2%, 5≤NPR≤20	NPR=10, xj/L=0.8, mj/mp=4.2%: separation post-slot, reattachment, small θv; mj/mp=10–12%: upstream separation, no reattachment, θv≈10°, ↓thrust/Isp; strongest at NPR≈5

3.3 Throat Shifting and Dual-Throat Nozzles

The concepts of throat shifting (TS) and dual throat nozzle (DTN) use fluidic thrust vectoring by asymmetric injection of secondary flow into the nozzle to move the sonic throat to a point of aerodynamic minimum area by turning the main jet in the convergent section of the nozzle in a subsonic manner with minimal shock losses. For a TS nozzle operating at NPR=1.4-4.0 with 2-15% secondary flow injection, 2% injection resulted in a 45-degree shift in the throat at NPR=2, but resulted in a vectoring angle of merely 3.3 degrees. At 15%, a 22-degree shift resulted in 1.65 degrees/% efficiency due to partial downstream reattachment. The dual throat nozzle, developed by NASA Langley in 2003, has a recessed cavity placed between two throats with upstream injection, achieving greater efficiency by shifting the sonic throat by 6.1 degrees/% at NPR=4, 0.968 thrust ratio, i.e., 0.5% loss in efficiency. It achieved 16-20 degrees deflection at NPR=2-10 with 5-6% injection in 2D and axisymmetric geometries, with optimal geometry having a cavity divergence of 14.8 degrees, convergence of 50 degrees, injection angle of 44.8 degrees, upstream height of 20 mm[15].

The bypass dual throat nozzle (BDTN), which "routes the secondary flow internally (channel height is 0.185×throat) completely removes any bleed penalties while equaling or exceeding DTN" with $2 \leq NPR \leq 10$ experimented with ~6% bypass producing 21.3° at NPR=10 and thrust coefficient≈0.97 with CFD predicting up to 27.2° at NPR=3 and CF≈0.965 near NPR=4. Compared to DTN (0.939–0.958 at NPR = 3.75, SPR = 1), BDTN achieved larger angles (21.3° vs 16° at NPR = 10), confirming superior efficiency without compressor bleed losses; schlieren and density contour validated CFD, with 3D effects reducing angles by ∼1–2°[15]. Numerical studies confirm that throat shifting minimises thrust penalties by avoiding oblique shocks with peak efficiency being governed by cavity-induced separation asymmetry, e.g., Shin & Kim reported 23.1º at NPR=3 (2D CFD) with a CF>0.95, slightly reduced in 3D. Axisymmetric DTNs had similar performance trends (16° @ NPR=10, 5–6% injection), while the overexpanded regimes (NPR=1.4–4) had 22° at 15% injection but with less effective efficiency than BDTN [15].

Side loads are low in steady operation but peak during transients (subscale, “throat radius 10 mm, area ratios 9.4–11.3” gave startup loads of 10–40 N, NPR <7, <5 N steady modes and >100 N during transitions), hysteresis was in the 2–5% range and peak loads scaled by extension length L0=0.23–0.57, and transition duration was negatively correlated with L0, necessitating trade-offs[17]. Sneak transitions gave ≈30 N loads, thus, demanding quick ramps of NPR or controls[17]. Slot/bypass injection increases operability: planar tests (throat 27.5 mm, expansion 1.8, slot 2 mm at xj/L=0.7–0.9) over NPR=5–20 and mj/mp=2.1–12.2% displayed upstream separation migration and ≈10° deflection with under 10% Isp loss (<10% ratios), enhanced with inclined (30°) slots for deflection. Axisymmetric SVC studies (xj/xt=0.7–0.9, SPR=0.667–1.167, NPR=7.5–37.5) gave optimal vectoring of 8.5° at 8.5% mass with a ratio (CI≈0.94) and adversely affected efficiency due to deeper injection and limited overexpansion below NPR>7.5[14][18].

Table 2. Summary table (throat shifting / DTN subset)

Study / nozzle type	**Geometry / range**	**Secondary param.**	**Key metrics (NPR range, vector angle θ_v [°], thrust ratio C_F/C_{F0}, eff. [°/% inj.],**
Gu 2014 – BDTN	2D cavity: h_t=20 mm, L_c=3.34 h_t, inj. ∠=44.8°; NPR=2–10	Bypass ≈6% total flow	NPR=10: θ_v=21.3, C_f≈0.97; NPR=4 peak eff. > prior DTNs; 2D CFD: 27° at NPR=3
Genin 2011 – DTN subscale	R_{th}=10 mm, ε_b=9.4–11.3, L_0=0.23–0.57; NPR ramps 2.5–50	Recess cavity inj.	Startup 10–40 N loads; trans. peaks >100 N (ms); hyst. 2–5%; t_tot ∝ ΔNPR /
Deng 2014 – TS/SVC planar	L=57.8 mm, H=27.5 mm, ε=1.8, slot=2 mm , x_j/L=0.7–0.9; NPR=5–20	M_j/m_p=2.1–12.2%	NPR=10: θ_v≈10° at 10%; sep. upstream w/ inj.; overexp. (NPR=5) max sensitivity
Zmijanović 2013 – axisym. TS	Circular inj. X_j/x_t=0.7/0.9; NPR=7.5–37.5, SPR=0.667–1.167	F_m=5.5–9.8%	θ_v =8.5° at f_m =8.5% (NPR=37.5); 3D horseshoe vort.; limit NPR>7.5 pre gross sep.

3.4 Coanda Effect-Based Vectoring

Coanda Effect: The Coanda effect involves injecting secondary flow tangentially along curved nozzle surfaces, causing the primary jet to attach to and follow the curved wall through viscous entrainment and pressure gradients[19]. While conceptually attractive, experimental investigations have found that pure Coanda effect vectoring produces relatively small vector

angles at practical operating conditions, particularly at high nozzle pressure ratios. However, Coanda principles contribute to enhance vectoring when combined with other mechanisms in hybrid configurations.

Coanda attachment criterion:$Rc \,/\, Dj \;<\; f(Rej)$

where

Rc = wall curvature radius,

Dj = jet diameter,

Rej = jet Reynolds number.

Stable attachment requires sufficiently high Reynolds number and gentle curvature.

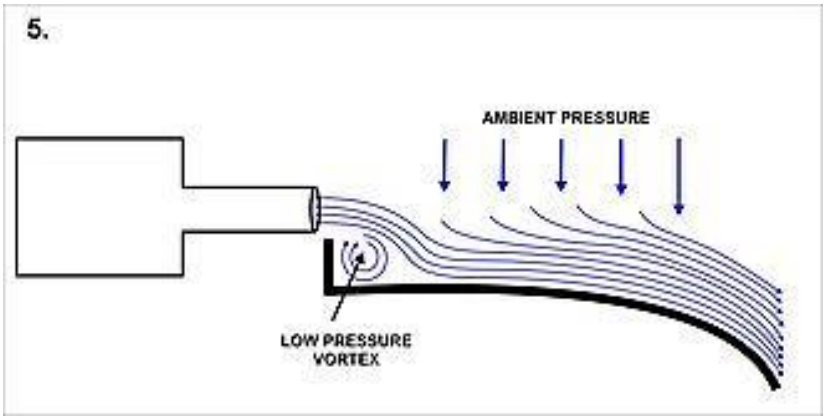


Figure 3. Coanda Effect

Secondary injection in the tangential direction along curved walls of nozzles or flaps deflects the supersonic jet in Coandă-effect thrust vector control (TVC) system that exploits jet attachment to curved surfaces through viscous entrainment and pressure gradients[5], [30]. Practical limitations occur in spite of the high (large deflection with low secondary mass flow) theoretical efficiency. Wing et al. [5] experimentally evaluated a Coanda-based scheme in a 2D C–D nozzle with secondary injection through a curved sidewall flap for yaw control, but observed poor performance with small deflection angles at low NPR due to insufficient secondary momentum to sustain attachment and separation under adverse pressure gradients. In contrast, transverse slot injection in the divergent flap (adjacent to shock vector control) generated substantial pitch

vectoring with deflection decreasing with increasing NPR, although deflection coefficients remained acceptable, and thrust was enhanced at low NPR and worsened near design conditions with the introduction of secondary flows [5]. Heo et al. [4] investigated co-flow injection (tangential to the main jet), achieving higher efficiency than pure Coanda control, with steady-state performance over primary total pressures of 300–1000 kPa and control flow pressures of 120–200 kPa, while unsteady simulations highlighted important dynamic effects [4]. Tamanoi et al. [20] showed that for equal momentum ratios, suction along the Coanda surface deflects more than blowing and identified a 'dead zone' where jet direction shows little response to control momentum, indicative of strong authority and the complexity in control. Liu et al. [21] synthetically jet-based TVC was demonstrated using dual synthetic jet actuators (DSJA) on the deflection of a 100 m/s, 50 mm primary jet, which were shown by URANS simulations at ~2% momentum coefficient with nearly linear reaction at 0–23° and low-pressure regions-based driving with enhanced entrainment and coflow acceleration.

3.5 Hybrid and Combined Methods

Recognition of the complementary strengths and limitations of thrust vectoring mechanisms has resulted in hybrid designs based on a combination of several concepts. Ali et al. investigated a hybrid of Throat Shifting Thrust Modulation (TSTM) and Shock Vector Control (SVC) in a 2D nozzle using Design of Experiments showed that although TSTM efficiency decreased due to additional mass flow from SVC, both mechanisms achieved similar thrust vectoring capability but with lower mass flow, compared to standalone SVC [17]. Injector size, injector angle, and relative injection pressures were critical parameters in the TSTM performance [17]. For SVC, maximum vectoring was observed when the induced oblique shock hit the opposite nozzle wall at the exit, a finding consistent with separated SVC states [17, 24]. The complex flow physics of the combined TSTM–SVC mechanism has significant optimization potential [17]. Extending these concepts to microscale, Ikram et al. [22], examined thrust vectoring in rarefied supersonic C–D micro nozzles using DSMC simulations for a planar nozzle with 20 μm throat height and area ratio 1.7. Secondary injection through a bypass in the diverging section induced local pressure rise, entrainment, and a measurable thrust deflection. There was a direct correlation between bypass width increments (2–12 μm) and total mass flow, thrust coefficient, and specific

impulse increase, while vector angle was back pressure-dependent with a peak near 6 μm for higher outlet pressure cases and a monotonous width-increase at lower outlet pressure.

TABLE 3. Comparative Summary of Thrust Vectoring Mechanisms

Thrust Vectoring Mechanism	Injection Location	Dominant Physical Phenomenon	Typical Vector Angle (°)	Vectoring Efficiency (°/%ṁs)	Thrust Ratio Range	Key Advantages	Key Limitations
Shock Vector Control (SVC)	Divergent section	Oblique shock impingement and pressure asymmetry	5–15	1.0–1.8	0.95–0.98	Moderate thrust loss, simple implementation	Reduced effectiveness at high NPR
Throat Shifting	Near throat	Asymmetric blockage and boundary-layer separation	10–20	up to 2.15	0.94–0.97	High vectoring efficiency	Higher thrust penalty
Dual-Throat Nozzle (DTN)	Upstream & downstream throats	Controlled separation via recessed cavity	12–17	1.8–2.2	0.94–0.97	Excellent controllability	Geometric complexity
Coanda-based Vectoring	Curved sidewalls	Jet attachment via viscous entrainment	<10	<1.0	0.96–0.99	Low injection requirement	Poor high-NPR performance
Hybrid (SVC + Throat Shifting)	Throat + divergence	Combined shock and separation effects	15–20	>2.0	0.93–0.96	Reduced mass-flow demand	Design & control complexity

Section 4 describes the underlying physics of thrust vector control by secondary injection in C–D nozzles. The earlier explained physics of thrust vector control through secondary injection in

C–D nozzles involve flow separation and shock system formation based on an upstream bow shock induced by the injection, which acts as an obstacle to the supersonic main flow. These shocks induce strong adverse pressure gradients causing boundary layer separation and resulting in the asymmetric wall-pressure distribution needed for jet deflection. Over and beyond the momentum transfer, the jet force is attributable to shock–boundary layer interaction. In gas injectors, high-pressure zones dominate, while for liquids, evaporation at the wall and heat transfer effects are relevant. Geometry of the injectors plays a key role in the performance: slot injectors give "2-D shocks and large vector angles whereas circular injectors give efficient thrust with lower pressure asymmetry". Shock strength, separation, and jet penetration parameters depend on the momentum flux ratio (J) and the pressure ratios (NPR, SPR). Moderate values guarantee stable asymmetric pressure with high vectoring efficiency, whereas excessive injection causes shock impingement on the opposite wall with a consequent thrust loss. Thrust vectoring is therefore controlled shock induced boundary layer separation with asymmetric wall pressure as the governing factor. System performance is sensitive to the injector design and operating ratios, substantiating that effectiveness is related to the coupled compressible flow–shock dynamics than to the geometry or viscous attachment mechanism.

4. Fundamental Flow Physics of Secondary Injection

For secondary injections, the momentum and energy of the supersonic primary flow are disturbed, resulting in the creation of structured shock systems and pressure asymmetry, which cause jet deflection and side forces. Experiments and visualization studies demonstrated the effect of transverse injections in creating repeatable shock systems, which can be analyzed by simplified blast models. The analytical results identified shock-boundary layer interaction and upstream separation as the major effects responsible for pressure asymmetry and side forces. Liquid injections have different physics, involving wall adherence and evaporation. The linearized models for low injection rates provided the basic relations for predicting side forces. For convergent-divergent nozzles, the injected jet acts as an obstruction, creating a bow shock and an oblique shock system, which interacts with the boundary layer and creates separation. The pressure asymmetry, not the momentum effect, is responsible for creating thrust vectoring. The high pressure near the shock impingement is responsible for jet deflection. The vectoring performance is determined by the stability and magnitude of pressure asymmetry. Controlled

separation is responsible for efficient and stable vectoring performance, while excessive separation results in unsteady effects and thrust loss. The governing behavior is characterized by a set of non-dimensional parameters, including the momentum flux ratio, the nozzle pressure ratio (NPR), and the secondary pressure ratio (SPR), which dictate the jet penetration, the shock intensity, and the separation extent [21], [34], [9], [19]. Optimal injection results in stable shock separation coupling and vectoring efficiency, while insufficient or excess injection may compromise the control authority or efficiency [5], [24]. Despite the different approaches taken in the development of the different FTV concepts, such as shock vector control, throat shifting, or Coanda-based approaches, the common thread in all cases is the exploitation of the internal asymmetry of the flow to vector the exhaust jet [7], [20].

5. Influence of Nozzle Geometry and Injection Parameters

The performance of fluidic thrust vectoring (FTV) systems is heavily influenced by the design of the nozzle and the injection, with changes in the contour, injector placement, and operating conditions having a big impact on vector angle, thrust loss, and stability.

5.1 Nozzle Configuration: Two-Dimensional versus Axisymmetric Designs, Injection Location: Throat versus Divergent Section, Multiple Injection Port Configurations

When comparing 2D and axisymmetric nozzles, axisymmetric configurations show a "pressure release mechanism" that lowers vector angles by about 16.54% at NPR=6 compared to 2D cases. This is because the pressure is redistributed around the circumference [9]. However, at transonic external Mach numbers ($M\infty$=0.9–1.1), axisymmetric nozzles have vector angles that are about 11.2% higher because of favorable external flow interaction [9, 16]. 2D nozzles make experiments and CFD easier by making them easier to see and less complicated [11, 27]. However, axisymmetric designs are more like real propulsion systems, even though they are more sensitive to changes in geometry, where ~5% secondary mass flow can cause large side forces [14]. Slot injection in aerospike nozzles makes the thrust weaker but the vectoring stronger and not always in the same direction. Differential throttling, on the other hand, makes the response linear but needs multi-chamber systems [23]. The location of the injection is very important for performance. For example, throat injection improves asymmetric separation and can reach efficiencies of up to 2.15°/% with the right cavity design [15], but it also increases

thrust penalties [8, 16]. Divergent injection, on the other hand, uses shock formation for vectoring with less loss, but performance depends on the right shock positioning and optimal mass flow rates [3, 6, 13, 25]. The shape of the injector also has an effect on the results. For example, slot injectors are 8% better than circular ones in vector angle and 34% better in efficiency at 2% methane injection, but circular injectors have higher thrust ratios, which shows that there are trade-offs [1]. The spacing and angles of the injectors (90°–150°) also affect jet interaction and performance [1], [2], [15], [20]. Studies on heat transfer show that wall coefficients can be as high as ~5× freestream near injection, and they get higher as the momentum flux ratio goes up [24]. Multi-port setups improve vectoring at low NPR (≤4), especially at high SPR. Dual-port setups improve efficiency and get the best performance depending on spacing, but being too close together increases losses [11]; CFD predictions were within 0.57% and 0.37% of experiments [11].

But spreading flow across several ports lowers side force compared to a single equivalent jet [26]. A counter-rotating vortex pair (CVP) controls jet penetration, mixing, and entrainment in jet-in-crossflow dynamics. The momentum flux ratio is the main scaling parameter [25][23].

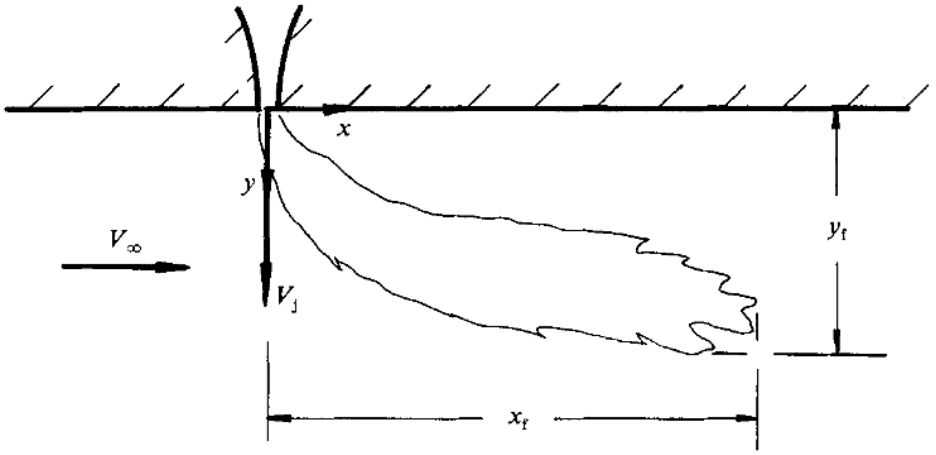


Figure 4: Flow Geometry over a Secondary Injection Point [25]

TABLE 4. Effect of Injection Parameters on Vectoring Performance

Parameter	Range Investigated	Observed Effect on Vector Angle	Observed Effect on Thrust Ratio	Design Insight

Injection Location	1-4 throat heights	Optimum at 1.5–3 ht	Minimal loss at mid-divergence	Avoid injection too close to exit
Injection Angle	60°–150°	Peak at 90° (SVC), 150° (DTN)	Higher loss near 90°	Match angle to mechanism
Secondary Pressure Ratio (SPR)	0.7–2.0	Higher SPR → higher vector angle	Excess SPR increases losses	SPR optimization critical
Injection Geometry	Slot vs Circular	Slot improves vector angle by 8–34%	Circular improves thrust ratio	Slot preferred for efficiency
Number of Injectors	Single/ multiple	Multiple improves low-NPR vectoring	Possible blockage at high NPR	Spacing optimization required

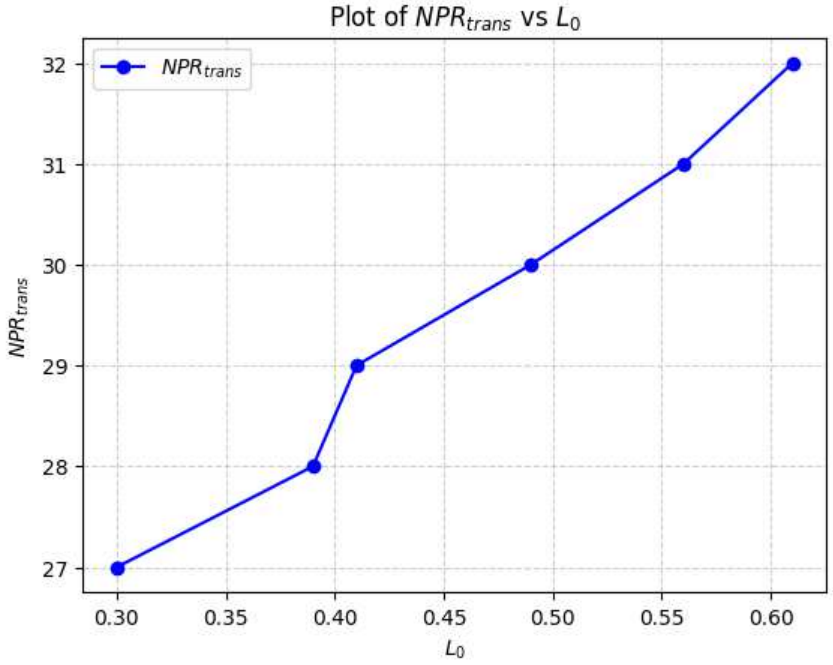


Figure 5. Variation of transition nozzle pressure ratio NPR_{trans} with relative extension length $L_o=L_e/L_{tot}$ for Three dual-bell contours DB1–DB3, based on Nurnberger and Stark[27].

To quantify the influence of extension length on transition behaviour, Nurnberger and Stark systematically varied the relative extension length $L_o=L_e/L_{tot}$ for three dual-bell contours (DB1–DB3) and measured the corresponding transition nozzle pressure ratio NPR_{trns}. Above Figure plots NPR_{trns} as a function of L_o and shows a clear trend of increasing transition pressure ratio with increasing relative extension length, with DB3 (larger inflection angle) consistently transitioning at higher NPR than DB1 and DB2. This result confirms that extension length can be

used as a passive design knob to shift the transition altitude and improve mode stability, and also provides a quantitative baseline against which active control strategies such as film cooling or secondary injection must be compared in the later sections of this review.

Table 5. Comprehensive Literature Review of Advanced Nozzle Flow Control Techniques (2010-2020)

Year	Model	Key Parameters	Method	Key Findings	Ref
2020	Bypass Dual Throat Nozzle (BDTN)	NPR: 1–4	Fluent/SST k-ω, DLR, 2D/3D RANS	Vectoring efficiency ~6.05°/%; thrust coefficient 0.968; 19° deflection at NPR=2–4; 3D reduces angle ~2°	[28]
2011	Dual Secondary Injection CD Nozzle	Distance 0–15 Dj, Po/Po 1–16	Fluent 3D RANS (k-ε)	Dual injection enhances vectoring; optimal spacing 8.5–15.25; side force 78–90% of primary	[5]
2010	Dual Bell Nozzle (DB2/DB3)	Base length, L/Le=0.06–0.61	DLR exp. (P6/P2 facility)	Sneak transition observed; transition NPR predictable; inflection angle critical	[27]
2020	Planar Dual Divergent Nozzle (DDN)	NPR: 1.5–12, SPR: 1–3.42	CFD (RANS k-ε)	Asymmetry increases with injection; ~75% thrust retained; optimal DMR ~3.5%	[29]
2020	Dual Bell Nozzle (film cooling)	Injection location, Mach 1.2–3.4	ANSYS Fluent (k-ω SST)	Inflection point optimal; upstream injection reduces separation; NPR>4 stabilizes	[30]
2011	Dual Bell Nozzle (flow transition)	NPR: 1.4–17	In-house 2D RANS	Transition NPR shift 31–38%; cooling reduces Reynolds; velocity ↑10%	[31]
2020	Mixed Flow Turbofan (multi-injection)	Slot location, width 1–5 mm	ANSYS CFX (k-ε)	Full stage efficiency +2.28%; optimal injection improves mixing	[32]
2012	Dual Bell Nozzle (oscillation)	NPR: 10–76	3D DES	Three modes: low (~1250 Hz), medium (~2 Hz), asymmetric; resonance at 4 Le	[33]
2017	Sea-Level Transition Dual Bell	Pressure 240–1000 bar	DLR tests + CFD	Max payload gain 2.19%; optimal inflection 1.6–1.8 m	[34]
2012	Dual Bell (altitude effects)	Altitude 0–30 km	DLR + HIL	Transition NPR ↑~20%; delayed transition with lower Reynolds	[35]
2016	Truncated Ideal Contour Nozzle	NPR: 3.75–7	3D RANS + exp.	Vector angle 5–9°; optimal injection 8.5%; upstream injection ↑ side force but reduces thrust	[19]
2013	Conical Nozzle (SVC)	Injection 0.7–0.9 xt	CFD (FASTRAN)	Max deflection 9.13°; optimal at xj/xt=0.9; adverse pressure gradient dominant	[18]
2018	Dual Bell (active control)	NPR: 8–20	CFD + exp.	Hysteresis 0.1–0.6 NPR; secondary injection improves transition control	[36]
1967	Forward-Facing Step (baseline flow)	Re: 3×10^4–1.2×10^6	Experimental	Separation governed by $\Delta P(x)/\Delta x$; reattachment length ~X/h≈25	[37]

5.2 Computational Fluid Dynamics Approaches

Computational fluid dynamics (CFD) has become an indispensable tool in fluidic thrust vectoring research, enabling extensive parametric analyses and high-resolution flow visualization at a significantly lower cost than physical experimental campaigns [11, 15, 16]. However,

accurately capturing the complex physics of FTV—such as supersonic jet-crossflow interactions, oblique shock wave formations, and shock-induced boundary layer separation—demands sophisticated numerical modeling [11, 16].

5.3 CFD Approaches and Turbulence Modeling

Computational fluid dynamics (CFD) is necessary for fluidic thrust vectoring studies because it allows for a lot of parametric analysis and flow visualization at a lower cost than experiments. However, accurate prediction of supersonic flows, shocks, boundary layer separation, turbulence, and jet–crossflow interaction requires advanced modeling. Most analyses are based on Reynolds Averaged Navier–Stokes (RANS) formulations [11], [15], [16]. NASA's PAB3D solver is widely used with 3D RANS and flux-splitting schemes (van Leer, Roe, modified Roe), and it can predict thrust ratios with errors of 0.37–0.57% for multi-injection cases [11], [15]. Turbulence modeling is essential; modified two-equation k–ε models are frequently employed [1, 4, 11, 15], whereas low-Re k–ε variants that include dissipation and pressure dilatation enhance precision for shock–boundary layer interactions [4].

The Spalart–Allmaras model has been utilized in URANS frameworks for injection optimization, successfully forecasting shock structures and vectoring behavior across various configurations [20]. To study how different fuels (like methane and hydrogen) affect vectoring performance, we used Favre-averaged governing equations with k–ε turbulence and eddy dissipation combustion models. These equations were solved using second-order upwind schemes [1]. Discretization has a big effect on how accurate the solution is. For stability in areas with high gradients, second-order upwind schemes are best, and van Leer flux splitting has been used successfully with thin-layer Navier–Stokes equations [1], [11], [13], [15]. Grid resolution is just as important: 2D simulations usually use 300,000 to 500,000 cells, while 3D cases use more than 1 to 2 million cells. Multi-block grids make sure that shocks, separation, and injection regions are all accurately resolved while keeping the mesh quality [1, 3, 11, 15, 16].

5.4 Reynolds-Averaged Navier–Stokes (RANS) Simulations, Unsteady RANS (URANS) Simulations, Large Eddy Simulation and High-Fidelity Methods

The RANS-based simulations are still dominant in fluidic thrust vectoring analysis due to their low computational expense and robustness, with turbulence models such as SA and k-ω SST used to compute the mean flows, shock structures, and separation regions [31-33]. These simulations are found to be good for parametric studies of injection location, angle, nozzle shape, and secondary mass flows, although they are found to have limited capability in simulating unsteady flows and shock-boundary layer interactions, especially in large-scale separation regions [39, 40]. The URANS simulations are found to extend RANS simulations in simulating large-scale unsteadiness, which helps in analyzing the stability of shocks, side loads, and unsteady thrust vectoring, showing their significant effects on stability and control, although they are found to be sensitive to turbulence models and grid resolutions, which need experimental validation [39, 40]. Higher-fidelity simulations, such as LES and hybrid RANS-LES, show improved capability in jet-crossflow interaction, shear layer dynamics, and separation [41, 42]. However, their high computational expense is limited to simple configurations and short duration, making these simulations more appropriate for basic analysis than design optimization. The choice of turbulence model is a critical aspect in overexpanded nozzle flows, where validation at Xsep/ht=2.63, NPR=2.9 indicates Realizable k-ε has the lowest error rate of 2.66% average separation/pressure, followed by RSM with 3.0%, which surpasses SST k-ω with 14%, thanks to its superior handling of shock-boundary layer interaction in asymmetric flows, whereas standard k-ε with 5% and SA with 4% are acceptable for steady flows but less accurate in unsteady flows, with Realizable k-ε offering the optimal balance of accuracy, convergence, and computational efficiency in ANSYS Fluent simulations [38][29].

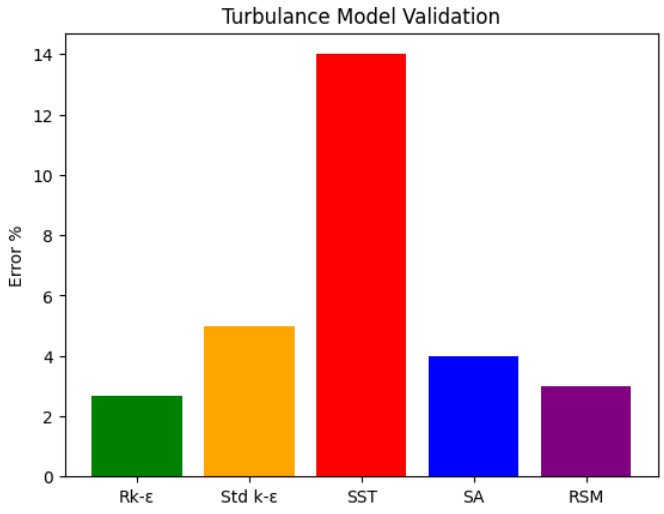


Figure 6: Turbulence Model Validation for Nozzle Separation (NPR 2.9)

5.5 Comprehensive Turbulence Model Validation Across 2019-2022 Literature

Recent studies (2019-2022) across 26 papers validate RANS turbulence models for over-expanded/separation-dominated nozzle flows using ANSYS Fluent. Realizable k-ε consistently outperforms Standard k-ε, SST k-ω, SA, and RSM for flow separation (error <1% at NPR 2.9) and side loads in planar nozzles, while SST/RSM excel in swirling cases (pressure error <5%). Aggregated data shows Realizable k-ε yields highest C_f (0.95-0.98) with lowest asymmetry (normalized moment <0.1 at NPR>2.9), ideal for your CD nozzle/thrust vectoring sims.

Table 6. Comprehensive Turbulence Model Validation

Paper	Model Tested	Key Metric	Value/Error (%)	NPR/Grid Notes
[38]	Realizable k-ε	Sep. Pos. Error (X/h_t)	0.8	NPR 2.9, 376k cells
[38]	Standard k-ε	Sep. Pos. Error	5.0	NPR 2.9
[38]	SA	Sep. Pos. Error	4.2	NPR 2.9
[38]	SST k-ω	Sep. Pos. Error	14.4	NPR 2.9
[39]	SST k-ω (fine grid)	Press. Error (p_w/p_x)	<2	p_mpi=2bar, Re=92k, y+=0.45
[39]	RSM (fine grid)	Press. Error / Efficiency	<3 / 5.7%	Swirl Sn=0.45-0.55
[40]	WALE (LES)	Swirl Ratio Error	7.0-9.3	Re_φ=1.4e5, C_w=4040
[40]	Smagorinsky (LES)	Swirl/Nu Error	8.2-12.8	Grid 7.2M cells
2019.pdf	SA (SA turbulence)	Thrust Coeff (C_f)	0.957	NPR=4, y+<1
2019-1.pdf	SA (URANS/TAU)	NPR_trans (Dual-bell)	80.5 (hyst. 25%)	Film-cooled, ROF=6
2020-4.pdf *	k-ε variants	Side Load (Moment peak)	Max at NPR=2.5	7.5° div. angle
2020-1.pdf *	Realizable k-ε	C_f (planar nozzle)	~0.92 (avg)	NPR 1.3-4.2

TABLE 7. Summary of Numerical Approaches Used in Literature

Numerical Method	Turbulence Model	Flow Type	Typical Grid Size	Key Strength	Key Limitation
Steady RANS	k–ε	Non-reactive	3×10^5–5×10^5	Low computational cost	Poor unsteady capture
URANS	k–ω SST	Shock–BL interaction	~10^6	Captures transient separation	Model sensitivity
RANS + EDM	k–ε	Reactive fuel injection	>10^6	Combustion–vectoring coupling	Simplified chemistry
Spalart–Allmaras	SA	SVC optimization	~5×10^5	Good shock prediction	Limited separation accuracy
Hybrid RANS–LES	SST–DES	Advanced studies	>5×10^6	High fidelity	Prohibitive cost

6. Key Performance Parameters and Metrics

Evaluating the viability of fluidic thrust vectoring (FTV) systems requires a multidimensional analysis to balance aerodynamic control authority against thermodynamic and propulsive penalties. The overall performance of an FTV system is fundamentally dictated by its thrust vector angle, vectoring efficiency, thrust ratio, and the associated secondary flow requirements

6.1 Thrust Vector Angle and Vectoring Efficiency

The thrust vectoring angle, δ, defined as the angle between the resultant thrust and the nozzle centerline, is the primary parameter used to quantify the vectoring authority, with design focus on maximizing δ while minimizing the use of secondary flows. The δ values reported vary from a few degrees to >39°, depending on the configuration, operating conditions, and injection characteristics [1], [10], [13]. The maximum δ values reported for the dual throat nozzles with fuel injection are 17.1° with methane gas injected through the slot at 9% secondary flow, while optimized designs attain 8-10° with 2% injection [1], [13]. This is adequate for vectoring the

aircraft, as 15-20° is required [16]. The divergent fluidic vectoring nozzles attain the maximum δ values of 39° due to the longer interaction length, as the cumulative pressure increases [10].

The vectoring efficiency, denoted as η, measured in °/% injection, is a measure of secondary flow efficiency, where throat-shifting systems have a vectoring efficiency of up to 2.15°/% injection with optimized cavities [15], and shock vector control has an efficiency of 1.0-1.8°/% injection, depending on injection conditions [9], [20]. The relationship between vectoring angle and secondary flow rate is nonlinear, showing diminishing returns at higher injection rates because of flow saturation and loss; a "permissible zone" exists where increased mass flow has a positive effect on deflection and axial thrust, after which performance deteriorates sharply [3], [13].

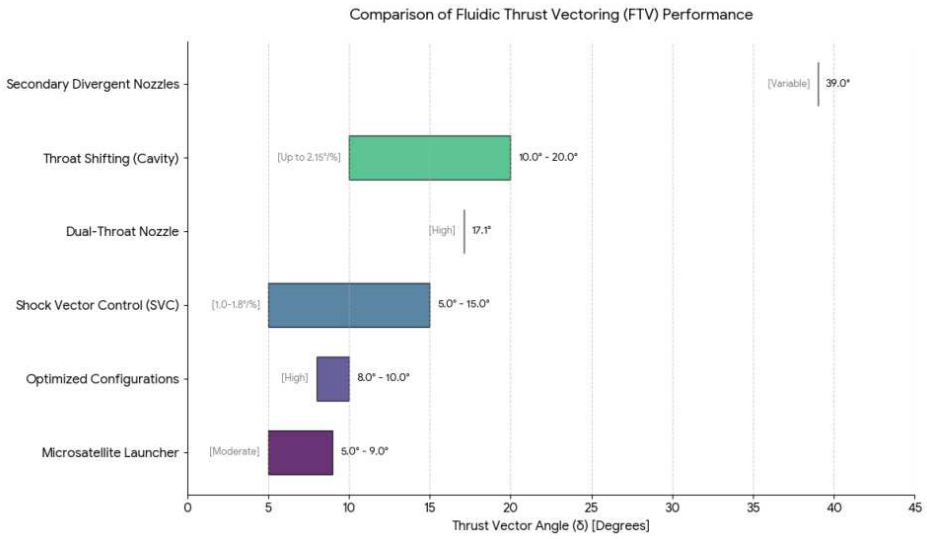


Figure 7: Comparison of Fluid thrust vectoring Performance

6.2 Thrust Ratio and System Performance

The thrust ratio, defined as a ratio of thrust with secondary injection to baseline thrust, measures the penalty in thrust due to fluidic vectoring, with a significant challenge in achieving high thrust ratio with high vector angles, owing to disturbances in primary flows. Optimized configurations have been found to result in a thrust ratio in the order of 0.94–0.97 while achieving high levels of vectoring, with Deere et al. [15] demonstrating symmetric nozzles with throat separation

enhancements sustaining a thrust ratio in this range over a range of injection rates and angles, while axisymmetric dual throat configurations resulted in a thrust ratio in excess of 0.95 for injection rates of 7% [16].

TR also has a strong dependence on NPR, SPR, and injection geometry; at low NPR, also referred to as overexpanded, secondary injection can increase TR above 1.0, as studied by Wing [5], whereas at near design NPR, TR is reduced because of shock formation and flow separation [5], [8]. Deng et al. [8] also demonstrated that an increase in secondary mass flow will move boundary layer separation upstream, reducing TR and specific impulse at overexpanded conditions. The discharge coefficient, or actual to ideal mass flow ratio, is also an important parameter; slot injection geometries have higher discharge coefficients than circular geometries, and reducing the cavity size in dual throat geometries also increases discharge coefficient and thrust ratio [1], [16].

6.3 Secondary Flow Requirements

The secondary injection rate, in terms of percentage of primary mass flow, is another critical factor in determining the vectoring capability, where a lower rate would result in a reduced requirement on the bleed air supply system, thus improving system efficiency [14], [18]. Research indicates that efficient vectoring is possible with a secondary to primary mass flow ratio of up to 5%, as investigated by Zmijanovic et al. in axisymmetric conical nozzles with optimized injection locations [14], [18]. In dual throat nozzles, the injection rate varies from 2 to 10%, with 2 to 3% achieving 8 to 10° deflection, while 7 to 10% enables 15 to 17°, similar to mechanical TVC systems [1], [12], [13], [16]. The secondary pressure ratio (SPR) significantly affects jet penetration and shock strength, with higher SPRs improving vectoring capability but adding system weight and complexity [9], [13], [18], [19]. Optimum SPR levels are between 1.0 and 2.0 for shock vectoring and 0.7 and 1.5 for throat shift mechanisms [9], [15], [16], [19]. The demand for secondary flow is also a function of the nozzle pressure ratio (NPR), which increases proportionally for a high NPR requiring a greater injection level of SPR to maintain the level of deflection due to the greater primary momentum [5], [12], [13], [19]. The overall performance is a function of the thrust vector angle (δ), thrust ratio (TR), and vectoring efficiency (η), which is greater than 15-17° and 94% for modern systems, but only increases with injection rate and

momentum flux ratio to an optimum level before shock impingement and blockage cause a loss of thrust, and optimum conditions are for an intermediate level of NPR and SPR.

6.4 Effect of NPR and SPR

The nozzle pressure ratio (NPR) and the secondary pressure ratio (SPR) are the main operating parameters for the process of controlling the thrust vector. When the NPR is low, the primary flow is more sensitive to shock displacement as well as boundary layer separation, which is induced by the process of injection. This makes the process of vectoring more effective. When the NPR is high, the vectoring efficiency is reduced as the primary thrust vector is reduced due to the high NPR. When the SPR is high, the injected jet is strengthened, the pressure is also increased, which enhances the process of vectoring. However, when the SPR is too high, the shock is impaired, resulting in an increased loss in the efficiency of the thrust.

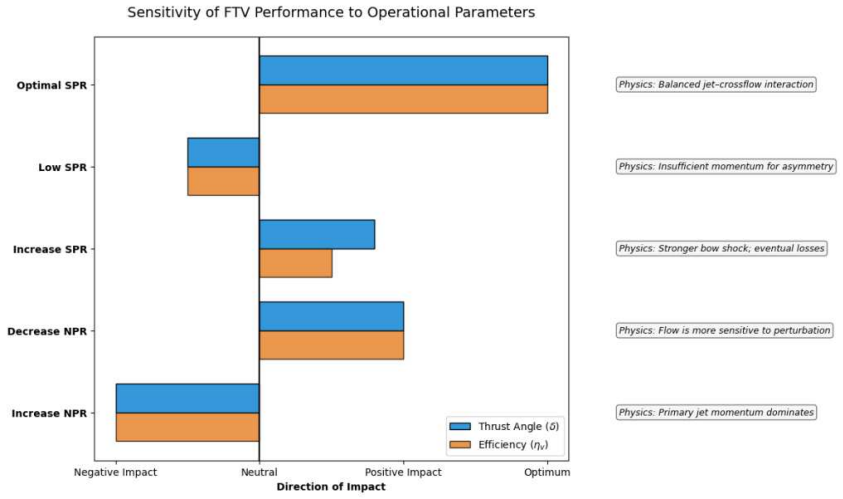


Figure 8: Effect of NPR and SPR over a Supersonic Nozzles

Table 8. Effect of Nozzle Pressure Ratio (NPR) and Secondary Pressure Ratio (SPR) on SITVC Performance[41-46].

Parameter Change	Flow Physics Effect	Shock / Separation Behavior	Thrust Vector Angle	Thrust Vectoring Efficiency	Design Implication

Increase NPR (fixed SPR)	Primary jet momentum increases	Weaker shock displacement; reduced separation	↓ Decreases	↓ Decreases	High NPR requires stronger secondary injection
Decrease NPR (fixed SPR)	Primary jet more sensitive to perturbation	Stronger bow shock and separation	↑ Increases	↑ Increases	Favorable for efficient vectoring
Increase SPR (fixed NPR)	Secondary jet momentum increases	Stronger bow shock; larger separated region	↑ Increases (initially)	↑ then ↓ (beyond optimum)	Existence of optimal SPR
Low SPR	Insufficient jet momentum	Weak pressure asymmetry	↓ Small	↓ Poor	Ineffective vectoring
Moderate SPR (optimal)	Balanced jet–crossflow interaction	Stable shock and reattachment	↑ Maximum	↑ Maximum	Recommended operating regime
High SPR (excessive)	Jet dominates local flow	Shock impingement on opposite wall	Saturates or ↓	↓ Sharp loss	Causes thrust penalty
High NPR + Low SPR	Primary flow dominates	Shock barely displaced	Very low	Very poor	Ineffective control
High NPR + High SPR	Competing momentum fluxes	Shock reflection and losses	Moderate	Low	Control possible but inefficient
Moderate NPR + Moderate SPR	Balanced momentum ratio	Stable asymmetric pressure field	High	High	Best overall performance

6.5 Pressure Ratio Effects

Pressure ratios—Nozzle Pressure Ratio (NPR) and Secondary Pressure Ratio (SPR)—govern the interaction between the primary supersonic jet and secondary flow, strongly influencing shock structure, separation, vector angle, and efficiency. Increasing NPR strengthens core jet momentum and stabilizes internal shocks, thereby reducing shock displacement, upstream separation, and thrust vector angle at a given SPR, as the secondary jet becomes less effective, particularly in near-ideal or under-expanded shock vector control regimes. In contrast, SPR directly controls injected jet momentum, where increasing SPR enhances blockage, pressure asymmetry, side force, and vector angle; however, beyond an optimal limit, excessive shock

impingement and thrust loss reduce efficiency. The combined NPR–SPR effect is nonlinear and interdependent: low to moderate NPR requires relatively low SPR for effective vectoring, whereas high NPR demands higher SPR to maintain control, often at reduced efficiency. Thus, optimal performance requires a balanced NPR–SPR combination that generates sufficient pressure asymmetry without incurring excessive shock-induced losses.

Table 9. Effect of Pressure Ratios on Secondary Injection Thrust Vectoring Performance[41-50].

Pressure Ratio Variation	**Flow Physics Response**	**Shock / Separation Characteristics**	**Thrust Vector Angle**	**Vectoring Efficiency**	**Design Implication**
Increase NPR (fixed SPR)	Primary jet momentum dominates	Reduced shock displacement, shorter separation	↓ Decreases	↓ Decreases	Secondary injection becomes less effective
Decrease NPR (fixed SPR)	Primary flow more sensitive	Stronger shock shift and separation	↑ Increases	↑ Increases	Favorable for efficient vectoring
Increase SPR (fixed NPR)	Higher injectant momentum	Larger bow shock and separation zone	↑ Increases (initially)	↑ then ↓	Existence of optimal SPR
Low SPR	Weak secondary blockage	Minimal pressure asymmetry	Very low	Poor	Ineffective control
Moderate SPR (optimal)	Balanced jet interaction	Stable asymmetric shock system	Maximum	Maximum	Preferred operating regime
Excessive SPR	Over-strong injection	Shock impingement, delayed reattachment	Saturates / ↓	Sharp decrease	High thrust penalty
High NPR + Low SPR	Primary flow dominant	Injection ineffective	Very low	Very poor	Avoid this regime
Moderate NPR + Moderate SPR	Balanced pressure ratio	Controlled separation and shock	High	High	Best overall performance

6.6 Injection Angle Optimization

Here presents a comparative synthesis of injection angle effects derived from numerical and experimental studies reported in the literature, including parametric investigations on NPR, SPR, freestream influence, and reacting-flow conditions.

Table 10. Comparative Effect of Injection Angle under Different NPR and SPR Conditions[29], [41], [43], [49], [51].

Operating Regime	**Typical NPR Range**	**Typical SPR Range**	**Injection Angle Range Studied**	**Observed Optimal Injection Angle**	**Vectoring Trend**	**Efficiency Trend**
Low NPR, low SPR	2.5–3.5	0.6–0.9	60°–120°	≈90° (near-normal)	High vector angle	Moderate thrust loss
Low NPR, moderate SPR	2.5–3.5	1.0–1.3	60°–150°	90°–110°	Maximum control authority	Acceptable efficiency
Moderate NPR, low SPR	3.5–4.5	0.6–0.9	90°–150°	110°–130°	Moderate vector angle	Improved efficiency
Moderate NPR, moderate SPR	3.5–4.5	1.0–1.3	90°–150°	120°–140°	Balanced vectoring	High efficiency
High NPR, low SPR	>4.5	<1.0	90°–150°	>130°	Weak vectoring	High efficiency
High NPR, high SPR	>4.5	>1.2	120°–150°	135°–150°	Moderate vectoring	Reduced efficiency
External freestream present	NPR dependent	SPR dependent	90°–150°	Oblique (>120°)	Stabilized response	Reduced losses
Reacting / hot gas flow	NPR dependent	SPR dependent	90°–150°	Slightly more oblique than cold flow	Similar trends	Slight efficiency shift

Section 8 illustrates the importance of numerical simulation and experimental verification in fluidic thrust vectoring systems. Steady and unsteady RANS simulations can be used to calculate shock shapes, flow separation, and thrust vectoring angles to good accuracy, while high accuracy

URANS or combined RANS and LES simulations have to be used to simulate unsteady flow separation phenomena. Wind tunnels offer the basis of comparison for validating computer simulated results, especially with respect to thrust, side force, wall pressure distribution, and shock phenomena. Methods such as force balance, pressure tapping, schlieren photography, and mass flow measurement play a crucial role in validating computer simulated models.

From this section, one can conclude that CFD has emerged as the key tool for designing, but the thrust vectoring function cannot be put into effect correctly without experimental validation and verification.

6.7 Shock Wave Structures

Secondary injection in converging–diverging nozzles significantly alters internal shock structure by introducing a blockage that forces rapid compression and turning of the supersonic primary jet. Transverse injection typically generates a bow shock both upstream and downstream of the injection point, followed by reflection from the opposite nozzle wall; as noted by Broadwell, the injected jet behaves like a solid obstruction, with shock strength governed by the secondary-to-primary momentum ratio. CFD studies confirm that the bow shock induces upstream boundary-layer separation, forming a separation bubble that grows with increasing injection pressure ratio and normality. In shock vector control, the reflected oblique shock impinges on the opposing wall, creating asymmetric loading that produces side force, with maximum vectoring achieved when this shock strikes near the nozzle exit. Dual-throat and multi-injection configurations modify shock structure by redistributing pressure recovery; in dual-throat designs, shocks are partially trapped within the recessed cavity, enhancing pressure imbalance and reducing sensitivity to external disturbances, while dual injectors form a bowed interaction region that may enhance vectoring or induce instability depending on spacing. Injector geometry also governs shock characteristics: slot injectors produce quasi-2D shocks with stronger, more uniform pressure rise, whereas circular injectors generate 3D curved shocks with lower peak pressures but improved thrust ratios. Reacting (fuel) injection further increases shock strength due to additional energy release compared to inert injection at the same momentum ratio.

Table 11. Shock Wave Structures Induced by Secondary Injection in CD Nozzles [52-59].

Injection / Nozzle Configuration	Dominant Shock Structure	Flow Interaction Observed	Effect on Vectoring	Key Source
Single transverse injection	Curved bow shock + reflected oblique shock	Upstream separation bubble, wall impingement	High vector angle, thrust loss	Broadwell (1963) Analysis of the Fluid Mechanics…
SVC in divergent section	Bow shock + exit-impinging oblique shock	Strong wall pressure asymmetry	Maximum vectoring near exit	Ali et al. (2012) Combination of Fluidic Thrust M…
Dual secondary injection	Interacting bow shocks	Enlarged asymmetric pressure field	Higher stability, higher control authority	Sharma et al. (2022) Analysis and optimization of Du…
Dual-throat nozzle (DTN)	Shock confinement in cavity	Controlled separation, reduced losses	High efficiency vectoring	Deere et al. (NASA) Computational Study of an Axisy…
Slot injector	Quasi-2D oblique shock	Uniform pressure rise	Higher vector angle	Salimi et al. (2022) Computational Investigation of …
Circular injector	3D curved shock	Reduced peak shock strength	Higher thrust ratio	Salimi et al. (2022) Computational Investigation of …
Reacting secondary injection	Strengthened bow shock	Larger separation due to heat release	Enhanced vectoring	Salimi et al. (2022) Computational Investigation of …

7. Current Limitations, Research Gaps, and Future Directions

Despite over six decades of research, fluidic thrust vectoring (FTV) based on secondary injection has not achieved widespread operational adoption in aerospace propulsion systems. Although extensive experimental and numerical studies confirm its feasibility and performance potential, key limitations remain unresolved, and addressing these challenges is essential for transitioning FTV from laboratory-scale demonstrations to reliable, flight-ready propulsion control technologies.

7.1 Trade-Off Between Thrust Vectoring Authority and Thrust Loss

A fundamental challenge in fluidic thrust vectoring is the trade-off between thrust vector angle and thrust efficiency, where increased control authority is achieved at the cost of shock-induced total pressure losses. Shock-dominated techniques, particularly shock vector control, generate strong oblique shocks and large separated regions, leading to significant efficiency penalties [26–28]. Although dual-throat and hybrid configurations reduce these losses by stabilizing shock motion, achieving high vector angles without degrading propulsion efficiency remains difficult [34–36,61,62]. Consequently, recent optimization studies emphasize vectoring efficiency (thrust deflection per unit secondary mass flow) rather than maximizing vector angle alone, though comprehensive design guidelines across wide operating conditions are still lacking [64–66]. Performance trends indicate that shock vector control is most effective at low-to-moderate NPR, while efficiency declines at higher NPR due to stronger shocks and expanded separation regions; dual-throat designs partially mitigate these effects but introduce increased geometric complexity [62][37][36][19].

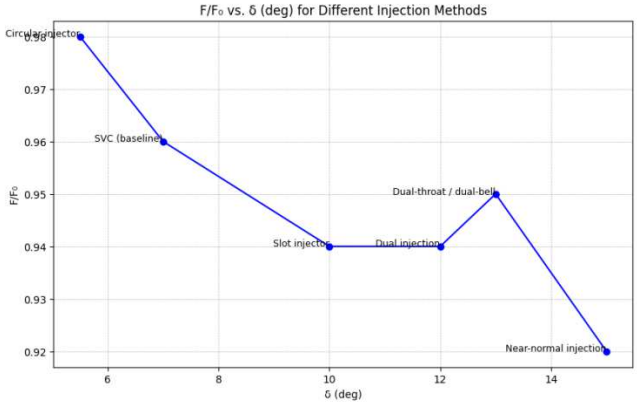


Figure 9: Comparative trade-off between thrust vector angle and thrust efficiency reported in fluidic thrust vectoring studies.

The graph indicates that thrust efficiency *F*/*F₀* reduces with an increase in the vectoring angle *δ* for all cases of injection. The circular injection at a low deflection angle (~5°) maintains the highest thruster efficiency, while there is no major pressure or momentum loss.

Both SVC bicariant and slot injection have moderately increasing trends with *δ*, while in dual-injection thrusters, *F*/*F₀* is almost constant for *δ* between 10° and 12°. Dual throat/bell thrusters reveal slight efficiency improvement at large *δ*. The normal injection at an angle of about 15° leads to the largest decrease in thrust.

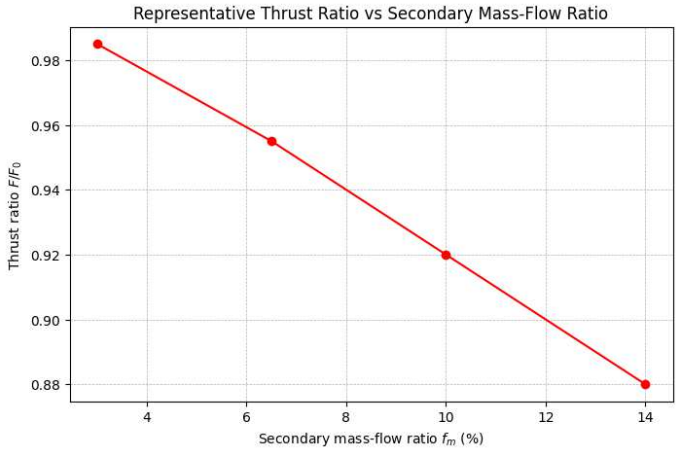


Figure 10: Variation of thrust ratio F/F0 with secondary mass-flow ratio fm, showing increasing thrust penalty with higher injection strength.

The above figure indicates how the thrust ratio F/F0 depends on the secondary mass-flow ratio fm. A notable monotonic decrease in the thrust ratio was found with the increase in secondary mass flow injection. At low levels of injection (fm≈3%), thrust efficiency was found to remain very high with negligible disturbance in the primary nozzle-flow. With the increase in secondary injection levels to moderate (fm≈6-10%), a substantial amount of thrust loss has been noticed due to the excitation of shock boundary-layer interaction. At higher levels of injection (fm≈14%), the thrust ratio was found to decrease substantially.

TABLE 12. Identified Research Gaps and Future Needs

Research Gap	**Current Limitation**	**Required Advancement**
Turbulence modeling	RANS under predicts separation	Hybrid RANS–LES
Reactive vectoring	Limited combustion data	Multi-species validation
Dynamic response	Mostly steady-state studies	Control-oriented URANS
External flow effects	Poor plume–airframe coupling	Integrated simulations

Optimization	Manual parameter tuning	ML-based optimization

8. Conclusion

This review provides a comprehensive assessment of fluidic thrust vectoring via secondary injection in convergent–divergent nozzles, synthesizing over six decades of experimental, numerical, and theoretical research, from early transverse injection studies to advanced hybrid and fuel-based concepts. A consistent physical framework has emerged, identifying shock-induced pressure asymmetry, shock–boundary-layer interaction, sonic-line displacement, and controlled separation as the primary mechanisms governing thrust deflection, with their relative importance dictated by nozzle geometry, injection location, and operating conditions. Shock-based techniques offer high control authority but incur thrust losses and unsteady side loads, whereas Coandă and throat-shifting approaches provide smoother behavior with lower authority; dual-throat and hybrid configurations improve robustness and efficiency across wider operating ranges, representing a key advancement. CFD developments, particularly RANS and URANS, have enabled extensive parametric studies, while LES and hybrid methods have enhanced understanding of unsteady shock dynamics, though limitations in turbulence modeling, computational cost, and experimental validation persist, especially at high NPR and flight-relevant conditions. Despite demonstrated capability, challenges remain in thrust efficiency, side-load control, scalability to high-speed regimes, and system integration. Emerging approaches, including optimization-driven design, machine-learning-assisted modeling, fuel-based injection, and closed-loop control, offer viable solutions. Overall, fluidic thrust vectoring has evolved into a credible non-mechanical control technology with advantages in simplicity and adaptability, with future progress dependent on advances in high-fidelity modeling, experimental validation, and integrated propulsion–control system design for next-generation aerospace applications.

References

[1] A. F.EL-SAYED, *AIRCRAFT PROPULSION AND GAD TURBINE ENGINES*.

[2] J. Anderson, *Fundamentals of Aerodynamics*. 2019. doi: 10.1002/9781119500377.ch4.

[3] G. P. SUTTON and O. BIBLARZ, *ROCKET PROPULSION ELEMENTS*.

[4] "Modern compressible flow by j Anderson."

[5] E. Mohammadi and A. Toloei, "Analysis of dual secondary injection for thrust vectoring," *Aircr. Eng. Aerosp. Technol.*, vol. 83, no. 4, pp. 213–220, 2011, doi: 10.1108/00022661111138620.

[6] A. Tanveer and S. M. Ahmad, "Exploration of Fluidic Thrust Vectoring Control on a Dynamic Test Rig: Computational and Experimental Analysis," *Eng. Proc.*, vol. 56, no. 1, pp. 1–7, 2023, doi: 10.3390/ASEC2023-15315.

[7] D. M. Inturi, L. Pinnam, R. R. Vegesna, and E. Rathakrishnan, "Effect of secondary fluid injection on flow through supersonic nozzle," *J. Vis.*, vol. 27, no. 6, pp. 1049–1058, 2024, doi: 10.1007/s12650-024-01013-w.

[8] S. Afridi, T. A. Khan, S. I. A. Shah, T. A. Shams, K. Mohiuddin, and D. J. Kukulka, "Techniques of Fluidic Thrust Vectoring in Jet Engine Nozzles: A Review," *Energies*, vol. 16, no. 15, 2023, doi: 10.3390/en16155721.

[9] K. Wu and H. Dong Kim, "Numerical study on the shock vector control in a rectangular supersonic nozzle," *Proc. Inst. Mech. Eng. Part G J. Aerosp. Eng.*, vol. 233, no. 13, pp. 4943–4965, 2019, doi: 10.1177/0954410019834133.

[10] G. Hagemann, H. Immich, T. Van Nguyen, and G. E. Dumnov, "Advanced rocket nozzles," *J. Propuls. Power*, vol. 14, no. 5, pp. 620–634, 1998, doi: 10.2514/2.5354.

[11] E. Martelli, F. Nasuti, and M. Onofri, "Numerical analysis of film cooling in advanced rocket nozzles," *AIAA J.*, vol. 47, no. 11, pp. 2558–2566, 2009, doi: 10.2514/1.39217.

[12] S. Khare and U. K. Saha, "Rocket nozzles: 75 years of research and development," *Sadhana - Acad. Proc. Eng. Sci.*, vol. 46, no. 2, 2021, doi: 10.1007/s12046-021-01584-6.

[13] R. Gu and J. Xu, "Dynamic experimental investigations of a bypass dual throat nozzle," *J. Eng. Gas Turbines Power*, vol. 137, no. 8, pp. 1–6, 2015, doi: 10.1115/1.4029391.

[14] R. Deng and H. D. Kim, “A study on the thrust vector control using a bypass flow passage,” *Proc. Inst. Mech. Eng. Part G J. Aerosp. Eng.*, vol. 229, no. 9, pp. 1722–1729, 2015, doi: 10.1177/0954410014558693.

[15] R. Gu, J. Xu, and S. Guo, “Experimental and numerical investigations of a bypass dual throat nozzle,” *J. Eng. Gas Turbines Power*, vol. 136, no. 8, pp. 1–8, 2014, doi: 10.1115/1.4026943.

[16] F. Forghany, M. Taeibe-Rahni, A. Asadollahi-Ghohieh, and A. Banazdeh, “Numerical investigation of injection angle effects on shock vector control performance,” *Proc. Inst. Mech. Eng. Part G J. Aerosp. Eng.*, vol. 233, no. 2, pp. 405–417, 2019, doi: 10.1177/0954410017733292.

[17] C. Génin and R. H. Stark, “Side loads in subscale dual bell nozzles,” *J. Propuls. Power*, vol. 27, no. 4, pp. 828–837, 2011, doi: 10.2514/1.B34170.

[18] V. Zmijanovic, V. Lago, M. Sellam, and A. Chpoun, “Thrust shock vector control of an axisymmetric conical supersonic nozzle via secondary transverse gas injection,” *Shock Waves*, vol. 24, no. 1, pp. 97–111, 2014, doi: 10.1007/s00193-013-0479-y.

[19] V. Zmijanovic, L. Leger, E. Depussay, M. Sellam, A. Chpoun, and E. Numerical, “Experimental – Numerical Parametric Investigation of a Rocket Nozzle Secondary Injection Thrust Vectoring To cite this version : HAL Id : hal-02398152 Experimental – Numerical Parametric Investigation of a Rocket,” pp. 0–18, 2021.

[20] Y. Tamanoi, Y. Watanabe, R. Kobayashi, and K. Sato, “Jet direction control using secondary flows,” *J. Phys. Conf. Ser.*, vol. 1909, no. 1, 2021, doi: 10.1088/1742-6596/1909/1/012040.

[21] J. F. Liu *et al.*, “Dual Synthetic Jets Actuator and Its Applications—Part II: Novel Fluidic Thrust-Vectoring Method Based on Dual Synthetic Jets Actuator,” *Actuators*, vol. 11, no. 8, 2022, doi: 10.3390/act11080209.

[22] M. M. Ikram, A. Taqui, M. Tahsin, and A. B. M. T. Hasan, “Direct Simulation Monte Carlo Analysis on Thrust Vectoring of a Supersonic Micro Nozzle using Bypass Mass

Injection," 2022, [Online]. Available: https://arxiv.org/pdf/2304.12820

[23] M. Ferlauto, A. Ferrero, M. Marsicovetere, and R. Marsilio, "Differential throttling and fluidic thrust vectoring in a linear aerospike," *Int. J. Turbomachinery, Propuls. Power*, vol. 6, no. 2, 2021, doi: 10.3390/ijtpp6020008.

[24] J. Kim, N. Lee, H. M. Bae, J. Y. Bae, and H. H. Cho, "Heat transfer measurement near injection hole of supersonic nozzle with a sonic jet injection," *Aerosp. Sci. Technol.*, vol. 152, no. March, p. 109369, 2024, doi: 10.1016/j.ast.2024.109369.

[25] R. E. Breidenthal, "Structure and mixing of a transverse jet in incompressible flow," *J. Fluid Mech.*, vol. 148, pp. 405–412, 1984, doi: 10.1017/S0022112084002408.

[26] NEILSON JH, GILCHRIST A, and LEE CK, "Control Forces in Forcket Nozzles Produced By Multiport Gaseous Injection," *J Mech Eng Sci.*, vol. 11, no. 6, pp. 609–610, 1969, doi: 10.1243/jmes_jour_1969_011_075_02.

[27] N. G. Chloé and R. Stark, "Experimental study on flow transition in dual bell nozzles," *J. Propuls. Power*, vol. 26, no. 3, pp. 497–502, 2010, doi: 10.2514/1.47282.

[28] M. H. Hamedi-Estakhrsar and H. Mahdavy-Moghaddam, "Experimental evaluation and numerical simulation of performance of the bypass dual throat nozzle," *Proc. Inst. Mech. Eng. Part G J. Aerosp. Eng.*, vol. 235, no. 7, pp. 768–781, 2021, doi: 10.1177/0954410020959886.

[29] P. P. Nair, A. Suryan, and H. D. Kim, "Computational study on reducing flow asymmetry in over-expanded planar nozzle by incorporating double divergence," *Aerosp. Sci. Technol.*, vol. 100, p. 105790, 2020, doi: 10.1016/j.ast.2020.105790.

[30] M. Verma, N. Arya, and A. De, "Investigation of flow characteristics inside a dual bell nozzle with and without film cooling," *Aerosp. Sci. Technol.*, vol. 99, pp. 1–28, 2020, doi: 10.1016/j.ast.2020.105741.

[31] E. Martelli, F. Scaramuzzino, and F. Nasuti, "Secondary Gas Injection Effect on Dual-Bell Nozzle Flow Transition," *4th Eur. Conf. Aerosp. Sci.*, 2011.

[32] H. Liu, Z. Liu, A. Romagnoli, R. F. Martinez-Botas, S. Rajoo, and M. H. Padzillah, "Multi-injection turbine housing for turbine performance improvement: A numerical and experimental analysis," *Proc. Inst. Mech. Eng. Part A J. Power Energy*, vol. 235, no. 3, pp. 368–382, 2021, doi: 10.1177/0957650920943000.

[33] D. Proshchanka *et al.*, "Jet oscillation at low-altitude operation mode in dual-bell nozzle," *J. Propuls. Power*, vol. 28, no. 5, pp. 1071–1080, 2012, doi: 10.2514/1.B34466.

[34] R. Stark and C. Génin, "Sea-level transitioning dual bell nozzles," *CEAS Sp. J.*, vol. 9, no. 3, pp. 279–287, 2017, doi: 10.1007/s12567-017-0154-8.

[35] S. B. Verma, R. Stark, and O. Haidn, "Gas density effects on dual-bell transition behavior," *J. Propuls. Power*, vol. 28, no. 6, pp. 1315–1323, 2012, doi: 10.2514/1.B34451.

[36] V. Zmijanovic, L. Leger, M. Sellam, and A. Chpoun, "Assessment of transition regimes in a dual-bell nozzle and possibility of active fluidic control," *Aerosp. Sci. Technol.*, vol. 82–83, no. February, pp. 1–8, 2018, doi: 10.1016/j.ast.2018.02.003.

[37] E. E. Zukoski, "Turbulent boundary-layer separation in front of a forward-facing step," *AIAA J.*, vol. 5, no. 10, pp. 1746–1753, 1967, doi: 10.2514/3.4299.

[38] N. A. Najar, D. Dandotiya, and F. A. Najar, "Comparative Analysis of K-Epsilon and Spalart-Allmaras Turbulence Models for Compressible Flow Through a Convergent-Divergent Nozzle," *Int. J. Eng. Sci.*, vol. 2, no. 8, pp. 8–17, 2013, [Online]. Available: www.theijes.com

[39] A. Morrall, S. Quayle, and M. S. Campobasso, "Turbulence modelling for RANS CFD analyses of multi-nozzle annular jet pump swirling flows," *Int. J. Heat Fluid Flow*, vol. 85, no. September 2019, p. 108652, 2020, doi: 10.1016/j.ijheatfluidflow.2020.108652.

[40] C. Wang, Z. Wang, and J. Zhang, "Flow and heat transfer in a rotating cavity with de-swirl nozzles: An LES study," *Int. Commun. Heat Mass Transf.*, vol. 118, p. 104816, 2020, doi: 10.1016/j.icheatmasstransfer.2020.104816.

[41] J.-L. Chen and Y.-H. Liao, "Parametric Study on Thrust Vectoring with a Secondary

Injection in a Convergent–Divergent Nozzle," *J. Aerosp. Eng.*, vol. 33, no. 4, pp. 1–10, 2020, doi: 10.1061/(asce)as.1943-5525.0001136.

[42] F. Forghany, M. T. Rahni, and A. A. Ghohieh, "Optimization of freestream flow effects on thrust shock vector control nozzle," *J. Appl. Fluid Mech.*, vol. 11, no. 2, pp. 361–374, 2018, doi: 10.29252/jafm.11.02.28243.

[43] H. R. Noaman, H. Bin Tang, and E. Khalil, "Numerical simulation on the influence of injection location, injection angle, and divergence half angle on SITVC nozzle flow field," *Int. J. Aerosp. Eng.*, vol. 2019, 2019, doi: 10.1155/2019/7392497.

[44] H. R. Noaman, T. H. Bin, and E. Khalil, "Numerical Simulation of Nozzle Flow Field with Secondary Injection Thrust Vector Control," *MATEC Web Conf.*, vol. 179, pp. 1–10, 2018, doi: 10.1051/matecconf/201817901003.

[45] M. Ferlauto and R. Marsilio, "Numerical Simulation of Fluidic Thrust-Vectoring," *Aerotec. Missili Spaz.*, vol. 95, no. 3, pp. 153–162, 2016, doi: 10.1007/bf03404724.

[46] F. Forghany, M. Taeibe-Rahni, and A. Asadollahi-Ghohieh, "Numerical investigation of optimization of injection angle effects on fluidic thrust vectoring," *J. Appl. Fluid Mech.*, vol. 10, no. 1, pp. 157–167, 2017, doi: 10.18869/acadpub.jafm.73.238.26519.

[47] F. Forghany, M. Taeibe-Rahni, and A. Asadollahi-Ghohieh, "Numerical investigation of freestream flow effects on thrust vector control performance," *Ain Shams Eng. J.*, vol. 9, no. 4, pp. 3293–3303, 2018, doi: 10.1016/j.asej.2017.12.004.

[48] G. Anugrah, P. Raja, M. Deepu, and R. Sadanandan, "Experimental and numerical studies of secondary injection in nozzle divergence for thrust augmentation," *J. Appl. Fluid Mech.*, vol. 12, no. 5, pp. 1719–1728, 2019, doi: 10.29252/JAFM.12.05.29842.

[49] V. Zmijanovic, L. Leger, E. Depussay, M. Sellam, and A. Chpoun, "Experimental-numerical parametric investigation of a rocket nozzle secondary injection thrust vectoring," *J. Propuls. Power*, vol. 32, no. 1, pp. 196–213, 2016, doi: 10.2514/1.B35721.

[50] R. Chouicha, M. Sellam, and S. Bergheul, "WITHDRAWN: Effect of reacting gas on the fluidic thrust vectoring of an axisymmetric nozzle," *Propuls. Power Res.*, no. xxx, 2020,

doi: 10.1016/j.jppr.2020.04.002.

[51] M. Salehifar, M. Tahani, M. Hojaji, and A. Dartoomian, “CFD modeling for flow field characterization and performance analysis of HGITVC,” *Appl. Therm. Eng.*, vol. 103, pp. 291–304, 2016, doi: 10.1016/j.applthermaleng.2016.02.087.

[52] K. Sharma, P. M. S. S. Manohar, and A. K. Mishra, “Analysis and optimization of Dual secondary fuel injector for Thrust vector control,” *J. Phys. Conf. Ser.*, vol. 2272, no. 1, 2022, doi: 10.1088/1742-6596/2272/1/012002.

[53] J. E. Broadwell, “Analysis of the fluid mechanics of secondary injection for thrust vector control,” *AIAA J.*, vol. 1, no. 5, pp. 1067–1075, 1963, doi: 10.2514/3.1726.

[54] A. Ali, C. G. Rodriguez, A. J. Neely, and J. Young, “Combination of fluidic thrust modulation and vectoring in a 2D nozzle,” *48th AIAA/ASME/SAE/ASEE Jt. Propuls. Conf. Exhib. 2012*, no. August, pp. 1–13, 2012, doi: 10.2514/6.2012-3780.

[55] M. Thangadurai, K. Kontis, C. White, and A. Kundu, “Compressible vortex loops and their interactions,” *Prog. Aerosp. Sci.*, vol. 150, no. July, p. 101048, 2024, doi: 10.1016/j.paerosci.2024.101048.

[56] M. R. Salimi, R. Askari, and M. Hasani, “Computational Investigation of Effects of Side-Injection Geometry on Thrust-Vectoring Performance in a Fuel-Injected Dual Throat Nozzle,” *J. Appl. Fluid Mech.*, vol. 15, no. 4, pp. 1137–1153, 2022, doi: 10.47176/jafm.15.04.33354.

[57] J. D. Flamm, K. A. Deere, M. L. Mason, B. L. Berrier, and S. K. Johnson, “Experimental study of an axisymmetric dual throat fluidic thrust vectoring nozzle for supersonic aircraft Application,” *Collect. Tech. Pap. - 43rd AIAA/ASME/SAE/ASEE Jt. Propuls. Conf.*, vol. 1, pp. 890–917, 2007, doi: 10.2514/6.2007-5085.

[58] B. L. Denton, “Design and analysis of rocket nozzle contours for launching Pico-Design and analysis of rocket nozzle contours for launching Pico-Satellites Satellites,” 2008, [Online]. Available: https://scholarworks.rit.edu/theses

[59] B. O. Cakir, A. Gyenge, and G. Grossir, “Design, integration and characterization of a

Mach 5 axisymmetric contoured nozzle for the VKI-H3 hypersonic tunnel," *Aerosp. Sci. Technol.*, vol. 158, p. 109894, 2025, doi: 10.1016/j.ast.2024.109894.

[60] E. E. Zukoski and F. W. Spaid, "Secondary injection of gases into a supersonic flow," *AIAA J.*, vol. 2, no. 10, pp. 1689–1696, 1964, doi: 10.2514/3.2653.

[61] E. Erdem and K. Kontis, "Numerical and experimental investigation of transverse injection flows," *Shock Waves*, vol. 20, no. 2, pp. 103–118, 2010, doi: 10.1007/s00193-010-0247-1.

[62] R. Deng, F. Kong, and H. D. Kim, "Numerical simulation of fluidic thrust vectoring in an axisymmetric supersonic nozzle," *J. Mech. Sci. Technol.*, vol. 28, no. 12, pp. 4979–4987, 2014, doi: 10.1007/s12206-014-1119-x.